

Structure of the *E. coli* ribosome–EF–Tu complex at $<3 \text{ \AA}$ resolution by C_s -corrected cryo-EM

Niels Fischer^{1*}, Piotr Neumann^{2*}, Andrey L. Konevega^{3,4,5}, Lars V. Bock⁶, Ralf Ficner², Marina V. Rodnina⁵ & Holger Stark^{1,7}

Single particle electron cryomicroscopy (cryo-EM) has recently made significant progress in high-resolution structure determination of macromolecular complexes due to improvements in electron microscopic instrumentation and computational image analysis. However, cryo-EM structures can be highly non-uniform in local resolution^{1,2} and all structures available to date have been limited to resolutions above 3 \AA ^{3,4}. Here we present the cryo-EM structure of the 70S ribosome from *Escherichia coli* in complex with elongation factor Tu, aminoacyl-tRNA and the antibiotic kirromycin at 2.65–2.9 \AA resolution using spherical aberration (C_s)-corrected cryo-EM. Overall, the cryo-EM reconstruction at 2.9 \AA resolution is comparable to the best-resolved X-ray structure of the *E. coli* 70S ribosome⁵ (2.8 \AA), but provides more detailed information (2.65 \AA) at the functionally

important ribosomal core. The cryo-EM map elucidates for the first time the structure of all 35 rRNA modifications in the bacterial ribosome, explaining their roles in fine-tuning ribosome structure and function and modulating the action of antibiotics. We also obtained atomic models for flexible parts of the ribosome such as ribosomal proteins L9 and L31. The refined cryo-EM-based model presents the currently most complete high-resolution structure of the *E. coli* ribosome, which demonstrates the power of cryo-EM in structure determination of large and dynamic macromolecular complexes.

Determining the structure of large, dynamic biological macromolecules at a uniformly high resolution provides a challenge both for X-ray crystallography and cryo-EM. Here we have used aberration-corrected cryo-EM in combination with extensive computational sorting to solve

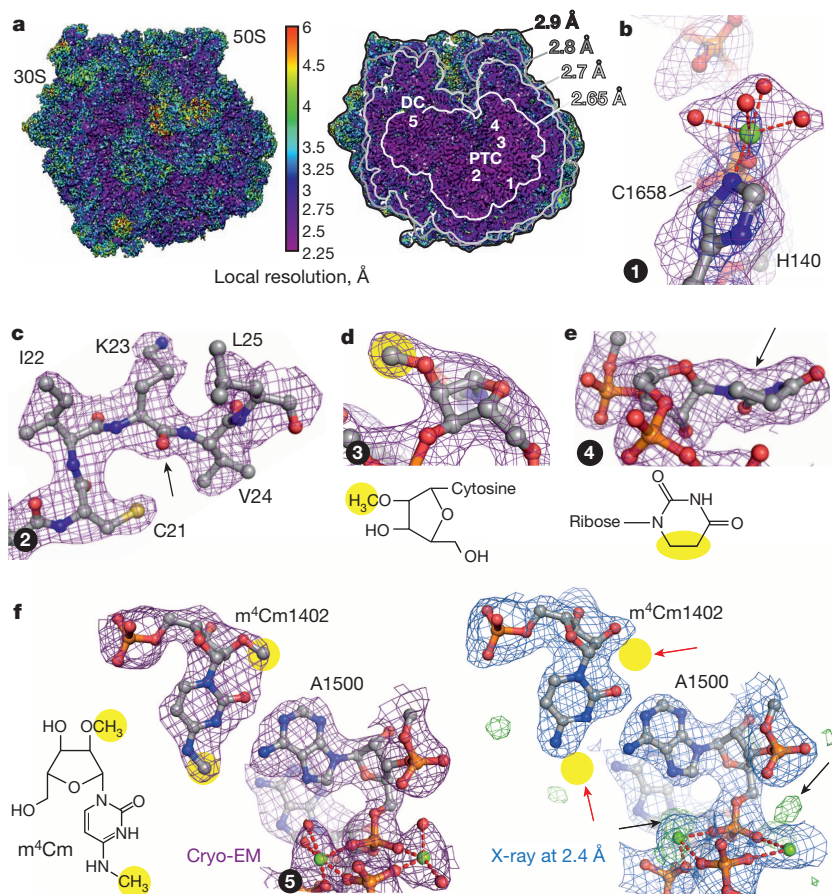


Figure 1 | High-resolution features of the cryo-EM map. **a**, 3D cryo-EM map of the kirromycin-stalled 70S–EF–Tu–Phe–tRNA^{Phe} complex from *E. coli* coloured according to local resolution. Left, surface view; right, cut-away view. PTC, peptidyl-transferase centre; DC, decoding centre. Numbers (1–5) mark the densities shown in **b–f** rendered at 3σ (purple mesh). **b**, Mg^{2+} ion (green) in octahedral coordination by four water molecules, C1658 of 23S rRNA and His 140 of the protein L3 (dark blue mesh, density at 6σ). **c**, Structure of the protein L14 revealing details such as the thiol group of Cys 21, the branched side chain of Ile 22, the zigzag pattern of Lys 23 side chain, and the carbonyl of the backbone (arrow). **d**, The 2'-O-methyl group (yellow) of Cm2498 in 23S rRNA. **e**, Nucleobase ring of D2449 in 23S rRNA with a characteristic distortion (arrow) of the planar geometry. **f**, The two methyl groups in $m^4\text{Cm}1402$ of 16S rRNA (yellow) resolved in the cryo-EM map (left), which are not seen (red arrows) in the X-ray map (right) of the 70S ribosome⁹ at 2.4 \AA (PDB ID: 4RB5; blue mesh, $2mF_o - DF_c$ map at 1σ). Non-built solvent molecules in the X-ray difference map are indicated by black arrows (green mesh, positive $mF_o - DF_c$ map at 3σ).

¹3D Electron Cryomicroscopy Group, Max-Planck-Institute for Biophysical Chemistry, Am Fassberg 11, 37077 Göttingen, Germany. ²Abteilung Molekulare Strukturbiologie, Institut für Mikrobiologie und Genetik, GZMB, Georg-August Universität Göttingen, Justus-von-Liebig-Weg 11, 37077 Göttingen, Germany. ³Molecular and Radiation Biophysics Department, B.P. Konstantinov Petersburg Nuclear Physics Institute of National Research Centre 'Kurchatov Institute', 188300 Gatchina, Russia. ⁴St Petersburg Polytechnic University, Polytechnicheskaya, 29, 195251 St Petersburg, Russia. ⁵Department of Physical Biochemistry, Max Planck Institute for Biophysical Chemistry, Am Fassberg 11, 37077 Göttingen, Germany. ⁶Department of Theoretical and Computational Biophysics, Max Planck Institute for Biophysical Chemistry, Am Fassberg 11, 37077 Göttingen, Germany. ⁷Department of 3D Electron Cryomicroscopy, Institute of Microbiology and Genetics, Georg-August Universität, 37077 Göttingen, Germany.

*These authors contributed equally to this work.

the structure of the *E. coli* 70S ribosome at high resolution to visualize rRNA modifications and dynamic parts of the ribosome. We prepared the 70S *E. coli* ribosome in the codon recognition state with the cognate ternary complex EF-Tu-GDP-Phe-tRNA^{Phe} stalled on the ribosome by the antibiotic kirromycin. Currently, a high-resolution crystal structure is available for the 70S-EF-Tu complex from *Thermus thermophilus* at 3.1 Å resolution⁶; however, a comparable structure of the complex from *E. coli* is still lacking, which makes it difficult to integrate structures with the results of biochemical, biophysical and genetic experiments, most of which were obtained with *E. coli* ribosomes. Cryo-EM images were recorded in a 300 kV electron cryo-microscope equipped with a spherical-aberration corrector and a direct electron detector operated in integration mode without alignment of intermediate image frames for motion correction. The aberration corrector was specifically tuned to reduce resolution-limiting aberrations and distortions (Extended Data Fig. 1). We applied a hierarchical classification strategy to sort the ribosome images computationally for the known modes of ribosomal motion and potential sources of heterogeneity in ribosome preparations (Extended Data Fig. 2)⁷. The final cryo-EM map at 2.9 Å overall resolution was subsequently used to refine the atomic model for the entire ribosome, including metal ions (Mg²⁺, Zn²⁺) and rRNA modifications (Methods and Extended Data Table 1). The local resolution map² is relatively uniform in resolution (Fig. 1a). For large portions of the map the resolution is better than 2.9 Å, whereas only few parts of the ribosome, located at the very periphery, are limited to resolutions >3.5 Å. Locally, average resolutions were 2.8 Å for 65%, 2.7 Å for 44% and 2.65 Å for 24% of the map, as determined by the crystallographic measures FSC_{work} (Fourier shell correlation) and CC_{work} (Pearson correlation coefficient)⁸ (Extended Data Fig. 3; see Methods for details). The final 3D map has a similar, or locally even better resolution compared to the available X-ray structures of the *E. coli* ribosome (Fig. 1 and Extended Data Fig. 4a). Also the structural definition of side chains as judged by local real-space correlations between the map and the model is similar to X-ray structures at comparable resolutions (Extended Data Table 2). In the best defined areas of the map Mg²⁺ ions can be visualized along with water molecules in the coordination sphere, indicating an optical resolution of at least 2.8 Å (Fig. 1b).

The present cryo-EM map visualizes for the first time modifications in rRNA, which were not observable in any of the high-resolution X-ray structures of the bacterial ribosome at 2.4–2.8 Å resolution^{5,9}, and were only seen in high-resolution X-ray structures of the *Haloarcula marismortui* 50S subunit at 2.2–2.4 Å resolution¹⁰ (Extended Data Fig. 4). In contrast, even single methyl groups of nucleosides can be clearly visualized in our cryo-EM map (Fig. 1d, f), as well as the non-planar base of dihydrouridine at position 2449 of 23S rRNA (Fig. 1e), while pseudouridines could be identified indirectly by polar residues within hydrogen-bonding distance of the N1 position. In total, we were able to build all 35 constitutive rRNA modifications¹¹ of the *E. coli* 70S ribosome.

The rRNA modifications are clustered at the main functional centres of the ribosome (Fig. 2 and Extended Data Fig. 5). Clusters of several rRNA modifications are essential for ribosome function, whereas individual rRNA modifications have an important role in fine-tuning the active centres of the ribosome, as well as in antibiotic resistance and sensitivity¹¹. Six individual rRNA modifications at the decoding centre modulate the efficiency and accuracy of translation initiation by stabilizing interactions in the P site^{12–14}. The present structure shows that the methyl group of m²G966 in 16S rRNA may act as a ‘backstop’ for the initiator tRNA, thereby stabilizing base-pairing with the initiation codon (Fig. 2b and Extended Data Fig. 5a; see Extended Data Fig. 5b for definition of rRNA modifications). The binding platform generated by m²G966 is further affected by base stacking interactions with the methyl group of m⁵C967. Messenger RNA binding to the P site is stabilized by an intricate network of interactions that involves four modified nucleotides. The P-site codon directly contacts m⁴Cm1402 and m³U1498 in 16S rRNA, which in turn are held in place by the bulky dimethylamine groups on m⁶₂A1519 and m⁶₂A1518. The network of long-range

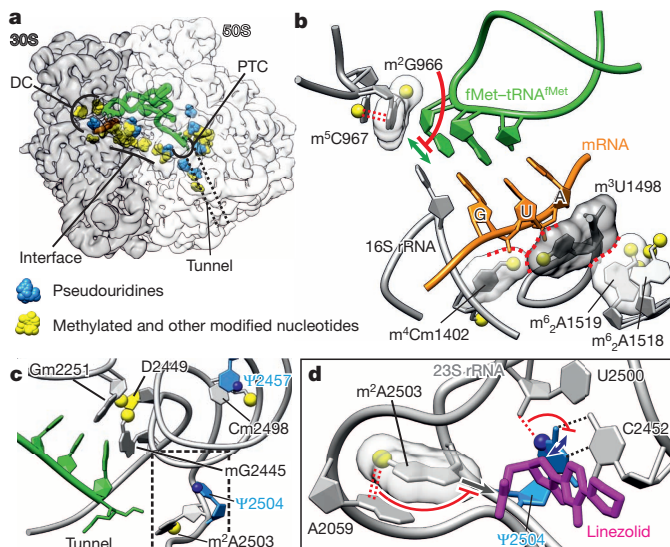


Figure 2 | Modifications of rRNA. **a**, Clusters of rRNA modifications (yellow and blue) at the functional centres of the ribosome. Initiator fMet-tRNA^{fMet} in the P site is shown in green. PTC, peptidyl-transferase centre; DC, decoding centre. **b**, Close-up of the decoding centre. Methyl group of m⁵C967 stacks onto the m²G966 base. The methyl group of m²G966 (yellow) restricts the mobility of the initiator tRNA (green). An interaction network of four modified nucleotides stabilizes the mRNA (orange) binding to the P site. **c**, Cluster of rRNA modifications in the peptidyl-transferase centre¹⁷. The essential Gm2251 forms a base pair with the P-site tRNA (green)²⁹; the dashed box indicates the part of the structure shown in **d**. **d**, rRNA modifications impacting antibiotic binding to the peptidyl-transferase centre. The stacking interaction of the A2503 methyl group with the base of A2059 stabilizes A2503 in a conformation compatible with binding of the antibiotic linezolid (magenta, superposition from PDB ID: 3CPW)³⁰. The nitrogen in Ψ2504 forms an additional hydrogen bond that stabilizes the nucleotide conformation.

interactions provides the basis for the action of the antibiotic kasugamycin, which binds in the P site and requires dimethylation of m⁶₂A1519 for its function¹⁵. In the A site of the decoding centre, the aminoglycoside class of antibiotics directly binds to a monomethylated residue, m⁵C1407 in 16S rRNA, which is needed for optimum drug activity¹⁶ (Extended Data Fig. 5c).

Assembly and peptidyl-transferase activity of the 50S subunit require a network of six modified nucleosides at the entry site of the peptide exit tunnel (Fig. 2c)¹⁷. Some of these modifications also modulate antibiotic sensitivity of the ribosome, which can now be explained at a structural level. For instance, resistance against the antibiotic linezolid caused by the loss of methylation of m²A2503¹⁸ can arise from the lack of stabilization by the m²A2503 methyl group on the stacking interaction with A2059, which keeps A2503 in a position that allows the antibiotic to bind. Conversely, the loss of the nitrogen at position 1 in Ψ2504 induces hypersensitivity against the antibiotics linezolid, tiamulin and clindamycin¹⁹, which can be due to the loss of interactions that stabilize Ψ2504 in a conformation less favourable for antibiotic binding (Fig. 2d). The present structure also rationalizes data on 23S rRNA modifications impacting intersubunit bridges and the peptide exit tunnel. For instance, a cluster of three pseudouridines (1911, 1915 and 1917) in helix 69, the central part of intersubunit bridge B2a, forms an enhanced stacking network, explaining their role in stabilizing the helix 69 structure (Extended Data Fig. 5c). The methyl group of m²G1835 has a pivotal role in shaping the junction of four 23S rRNA helices (67–70) which, in turn, directly face 16S rRNA and form intersubunit bridges B2b and B2c (Extended Data Fig. 5d), in line with data showing that this methyl group affects subunit association and cell fitness under stress conditions²⁰. A cluster of four modifications (m¹G745, Ψ746, m⁵U747 and m⁶A1618) lines the peptide exit tunnel (Extended Data Fig. 5e), of which m⁶A1618 has been shown to be important for cell growth and fitness²¹. Notably,

m⁶A1618 and its direct environment have also been recently predicted as the most promising novel drug target by a computational approach²².

Generally, obtaining uniform resolution for large macromolecules and especially for bound factors is difficult for cryo-EM^{1,2} and X-ray crystallography^{23–25}, because of mobility and/or occupancy problems. Owing to extensive computational sorting of images, our cryo-EM map is comparable in local resolution variations to crystallographic maps. Higher B factors in X-ray structures are also in line with structural elements exhibiting the highest mobility in molecular dynamics simulations (Extended Data Fig. 6), suggesting that structural dynamics is the prevailing factor limiting local resolution. In X-ray crystallography, those flexible regions may be resolved when stabilized by crystal packing interactions. In cryo-EM, however, computational sorting of images can be employed to improve the local resolution of dynamic structural features. In the cryo-EM map, the local resolution of the EF-Tu-GDP-kirromycin-Phe-tRNA^{Phe} complex was improved by sorting for ligand occupancy, resulting in a well-defined density at only slightly lower local resolution compared to the ribosome core. Notably, we find a clear density for the antibiotic kirromycin (Fig. 3a), underlining the power of

computational sorting in cryo-EM. Whereas the overall architecture of the EF-Tu-GDP-kirromycin-Phe-tRNA^{Phe} complex is similar to that reported by X-ray crystallography^{6,26}, there are local differences in the conformation of the distorted tRNA in the A/T state, in the orientation of the catalytic His84 residue and in the interactions between domain 2 of EF-Tu and the 30S subunit (Extended Data Fig. 7). Importantly, a shift in domain 2 (residues 219 to 226) of EF-Tu upon ribosome binding appeared crucial for distortion of the 3' end of tRNA and, ultimately, GTPase activation²⁶. The cryo-EM structure shows a similar distortion of the tRNA, but different interactions of EF-Tu domain 2, indicating that the reported changes in domain 2 may not be essential for the mechanism of catalytic activation. The highly mobile protein L9 is stabilized in crystals in an extended conformation by contacts to a neighbouring ribosome in the crystal lattice (Fig. 3b). In cryo-EM structures, this stabilization is absent and usually only the amino-terminal domain of the protein is structurally well-defined. Nevertheless, we were able to build the complete model for the conformation of L9 on the ribosome in solution, which reveals the contacts of L9 to the 30S subunit (Fig. 3b, c and Extended Data Fig. 8a). Notably, both conformations

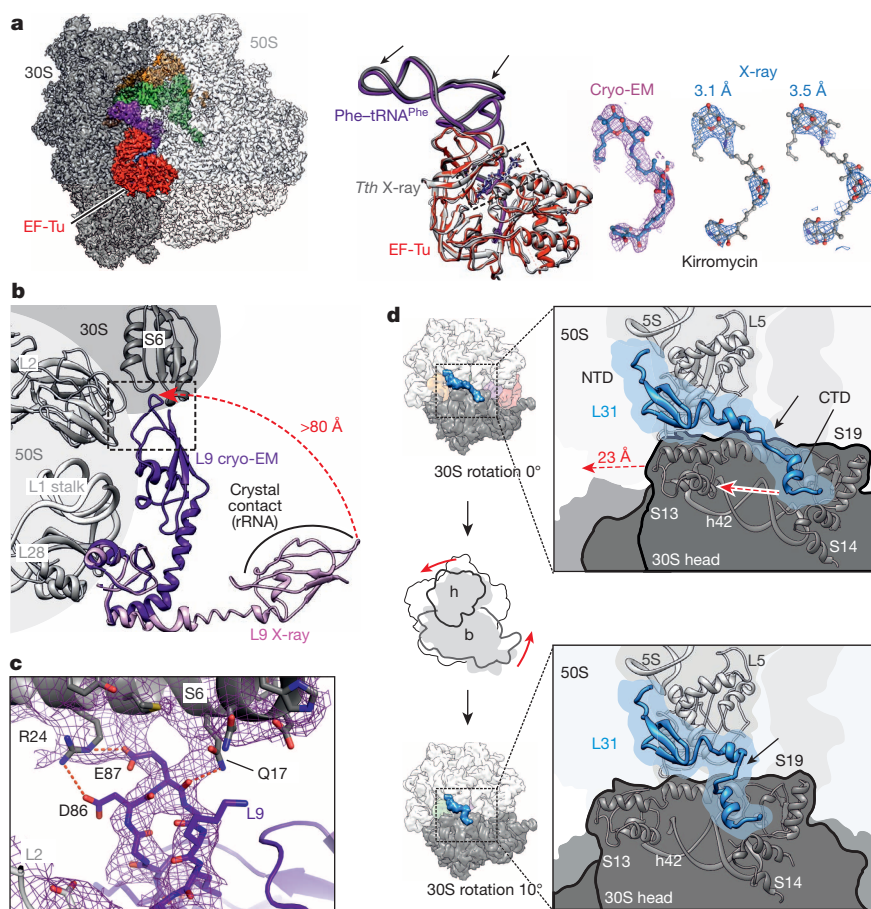


Figure 3 | Structure of ribosome ligands and mobile elements. Overview of the ribosome-EF-Tu complex. Left, cryo-EM map filtered to the local resolution of the factor binding site (3.1 Å). EF-Tu (red), the antibiotic kirromycin (blue), Phe-tRNA^{Phe} in the A/T state (purple), fMet-tRNA^{fMet} in the P site (green) and deacylated tRNA^{fMet} in the E site (orange) are shown. Centre, comparison of the present structure with the X-ray structure of the kirromycin-stalled complex from *T. thermophilus* (*Tth*) with Trp-tRNA^{Trp}, PDB ID: 2Y18 (grey)⁶. Differences in tRNA structures are indicated by arrows, the dashed box shows the position of kirromycin. Right, comparison of experimental densities for kirromycin in this cryo-EM map (left) and crystallographic maps determined at 3.1 Å (centre, PDB ID: 2Y18)⁶ and 3.5 Å resolutions (right, PDB ID: 2WRN²⁶). The cryo-EM map filtered to the local resolution of about 3.4 Å is shown at 1.5 σ (magenta mesh), the X-ray 2mF_o-DF_c maps at 1 σ (blue mesh). **b**, Protein L9 on the ribosome. L9 in a bent

conformation with the carboxy-terminal domain (CTD) contacting ribosomal proteins (L9 cryo-EM, purple) versus the elongated L9 in crystal structures (L9 X-ray, pink, PDB ID: 4TP9⁹). In crystals, L9-CTD interacts with the 16S rRNA of a neighbouring ribosome rather than the 30S subunit of the same ribosome. **c**, Close up of L9-ribosome interactions marked by the dashed box in **b**. **d**, Coupling between L31 motions and global ribosome dynamics. Top, L31 in the non-rotated codon-recognition state of the ribosome with EF-Tu and three tRNAs bound. 5S, 5S rRNA; h42, helix 42 of 16S rRNA; NTD, N-terminal domain. Bottom, L31 in the rotated state of the ribosome with two tRNAs in hybrid states. L31 accommodates the large-scale rearrangements of the ribosome using its flexible linker region (black arrows), while preserving its binding sites on the ribosome. Mid left, schematic depicting the ratcheting of head (h) and body (b) of the 30S subunit.

of L9 observed in cryo-EM and crystals appear to be compatible with the binding of elongation factors to neighbouring ribosomes in polyosomes as determined by cryo-electron-tomography²⁷ (Extended Data Fig. 8c). Furthermore, we built the model for L31, which is missing in the available *E. coli* 70S X-ray structures, probably owing to its dynamic nature. L31 bridges the ribosome at the top of the 30S head and the central protuberance of the 50S subunit. Upon 30S subunit ratcheting, the linker region of L31 switches from an extended to a kinked conformation, while L31 maintains its interactions with both subunits (Fig. 3d). We visualized this structural rearrangement by analysing another cryo-EM map of the ribosome with tRNAs in hybrid states (Extended Data Fig. 8b). The low occupancy of L31 can be explained by its flexible binding mode, which may also be important for the function of L31 as a Zn²⁺ reservoir for the cell²⁸.

In conclusion, our data shows that aberration-corrected cryo-EM allows dynamic macromolecular machines, such as the ribosome, to be visualized at a uniform resolution better than 3 Å with only small variations in local resolution. The ‘purification’ of electron microscopic images by computational sorting appears to be as powerful as the purification of ribosome conformation and composition during crystal growth in X-ray crystallography. The cryo-EM map visualizes bound water molecules, ions and rRNA modifications, providing novel insights into ribosome and antibiotic function, and thereby contributing to an improved structural basis for the development of new antibiotics.

Online Content Methods, along with any additional Extended Data display items and Source Data, are available in the online version of the paper; references unique to these sections appear only in the online paper.

Received 21 November 2014; accepted 30 January 2015.

Published online 23 February 2015.

- Leschziner, A. E. & Nogales, E. Visualizing flexibility at molecular resolution: analysis of heterogeneity in single-particle electron microscopy reconstructions. *Annu. Rev. Biophys. Biomol. Struct.* **36**, 43–62 (2007).
- Kucukelbir, A., Sigworth, F. J. & Tagare, H. D. Quantifying the local resolution of cryo-EM density maps. *Nature Methods* **11**, 63–65 (2014).
- Yu, X., Ge, P., Jiang, J. S., Atanasov, I. & Zhou, Z. H. Atomic model of CPV reveals the mechanism used by this single-shelled virus to economically carry out functions conserved in multishelled reoviruses. *Structure* **19**, 652–661 (2011).
- Wong, W. *et al.* Cryo-EM structure of the *Plasmodium falciparum* 80S ribosome bound to the anti-protozoan drug emetine. *eLife* **3**, e03080 (2014).
- Noeske, J. *et al.* Synergy of streptogramin antibiotics occurs independently of their effects on translation. *Antimicrob. Agents Chemother.* **58**, 5269–5279 (2014).
- Schmeing, T. M., Voorhees, R. M., Kelley, A. C. & Ramakrishnan, V. How mutations in tRNA distant from the anticodon affect the fidelity of decoding. *Nature Struct. Mol. Biol.* **18**, 432–436 (2011).
- Fischer, N., Konevega, A. L., Wintermeyer, W., Rodnina, M. V. & Stark, H. Ribosome dynamics and tRNA movement by time-resolved electron cryomicroscopy. *Nature* **466**, 329–333 (2010).
- Karplus, P. A. & Diederichs, K. Linking crystallographic model and data quality. *Science* **336**, 1030–1033 (2012).
- Polikanov, Y. S. *et al.* Amicoumacin A inhibits translation by stabilizing mRNA interaction with the ribosome. *Mol. Cell* **56**, 531–540 (2014).
- Schmeing, T. M., Huang, K. S., Kitchen, D. E., Strobel, S. A. & Steitz, T. A. Structural insights into the roles of water and the 2′ hydroxyl of the P site tRNA in the peptidyl transferase reaction. *Mol. Cell* **20**, 437–448 (2005).
- Sergiev, P. *et al.* in *Ribosomes* (eds Rodnina, M. V., Wintermeyer, W. & Green, R.) Ch. 9, 97–110 (Springer Vienna, 2011).
- Burakovskiy, D. E. *et al.* Impact of methylations of m²G966/m⁵C967 in 16S rRNA on bacterial fitness and translation initiation. *Nucleic Acids Res.* **40**, 7885–7895 (2012).
- Das, G. *et al.* Role of 16S ribosomal RNA methylations in translation initiation in *Escherichia coli*. *EMBO J.* **27**, 840–851 (2008).
- Kimura, S. & Suzuki, T. Fine-tuning of the ribosomal decoding center by conserved methyl-modifications in the *Escherichia coli* 16S rRNA. *Nucleic Acids Res.* **38**, 1341–1352 (2010).
- Schuwirth, B. S. *et al.* Structural analysis of kasugamycin inhibition of translation. *Nature Struct. Mol. Biol.* **13**, 879–886 (2006).
- Gutierrez, B. *et al.* Fitness cost and interference of Arm/Rmt aminoglycoside resistance with the RsmF housekeeping methyltransferases. *Antimicrob. Agents Chemother.* **56**, 2335–2341 (2012).
- Green, R. & Noller, H. F. *In vitro* complementation analysis localizes 23S rRNA posttranscriptional modifications that are required for *Escherichia coli* 50S ribosomal subunit assembly and function. *RNA* **2**, 1011–1021 (1996).
- LaMarre, J. M., Howden, B. P. & Mankin, A. S. Inactivation of the indigenous methyltransferase RlmN in *Staphylococcus aureus* increases linezolid resistance. *Antimicrob. Agents Chemother.* **55**, 2989–2991 (2011).
- Toh, S.-M. & Mankin, A. S. An indigenous posttranscriptional modification in the ribosomal peptidyl transferase center confers resistance to an array of protein synthesis inhibitors. *J. Mol. Biol.* **380**, 593–597 (2008).
- Osterman, I. A. *et al.* Methylated 23S rRNA nucleotide m²G1835 of *Escherichia coli* ribosome facilitates subunit association. *Biochimie* **93**, 725–729 (2011).
- Sergiev, P. V., Serebryakova, M. V., Bogdanov, A. A. & Dontsova, O. A. The ybiN gene of *Escherichia coli* encodes adenine-N6 methyltransferase specific for modification of A1618 of 23S ribosomal RNA, a methylated residue located close to the ribosomal exit tunnel. *J. Mol. Biol.* **375**, 291–300 (2008).
- David-Eden, H., Mankin, A. S. & Mandel-Gutfreund, Y. Structural signatures of antibiotic binding sites on the ribosome. *Nucleic Acids Res.* **38**, 5982–5994 (2010).
- Burnley, B. T., Afonine, P. V., Adams, P. D. & Gros, P. Modelling dynamics in protein crystal structures by ensemble refinement. *eLife* **1**, e00311 (2012).
- Schröder, G. F., Levitt, M. & Brunger, A. T. Deformable elastic network refinement for low-resolution macromolecular crystallography. *Acta Crystallogr. D* **70**, 2241–2255 (2014).
- Kleywegt, G. J. Crystallographic refinement of ligand complexes. *Acta Crystallogr. D* **63**, 94–100 (2007).
- Schmeing, T. M. *et al.* The crystal structure of the ribosome bound to EF-Tu and aminoacyl-tRNA. *Science* **326**, 688–694 (2009).
- Brandt, F. *et al.* The native 3D organization of bacterial polysomes. *Cell* **136**, 261–271 (2009).
- Akanuma, G., Nanamiya, H., Natori, Y., Nomura, N. & Kawamura, F. Liberation of zinc-containing L31 (RpmE) from ribosomes by its paralogous gene product, YtiA, in *Bacillus subtilis*. *J. Bacteriol.* **188**, 2715–2720 (2006).
- Samaha, R. R., Green, R. & Noller, H. F. A base pair between tRNA and 23S rRNA in the peptidyl transferase centre of the ribosome. *Nature* **377**, 309–314 (1995).
- Ippolito, J. A. *et al.* Crystal structure of the oxazolidinone antibiotic linezolid bound to the 50S ribosomal subunit. *J. Med. Chem.* **51**, 3353–3356 (2008).

Acknowledgements We thank F. Würriehausen for expert technical assistance and M. Lüttich and B. Busche for support in high-performance computation and programming. The work was supported by the Deutsche Forschungsgemeinschaft Grant FOR 1805 (to H.S. and M.V.R.) and by the Sonderforschungsbereich 860 (to H.S., R. F., and M.V.R.).

Author Contributions N.F. designed and performed cryo-EM experiments and data analysis. P.N. conceived and performed pseudo-crystallographic refinement and model validation and analysed data. A.L.K. prepared ribosome complexes. L.V.B. performed and analysed molecular dynamics simulations. All authors discussed the results. H.S. and N.F. conceived the project and wrote the paper with input from all authors.

Author Information The 2.9 Å cryo-EM map of the *E. coli* ribosome–EF-Tu complex has been deposited in the Electron Microscopy Data Bank with accession code EMD-2847, the coordinates of the atomic model have been deposited in the Protein Data Bank under accession code 5AFI. Reprints and permissions information is available at www.nature.com/reprints. The authors declare no competing financial interests. Readers are welcome to comment on the online version of the paper. Correspondence and requests for materials should be addressed to N.F. (niels.fischer@mpibpc.mpg.de) or H.S. (hstark1@gwdg.de).

METHODS

Complex preparation. To obtain kirromycin-stalled *E. coli* ribosome–EF–Tu complexes, ribosomes from *E. coli* MRE 600, initiation factors (IF1, IF2, IF3), fMet–tRNA^{fMet}, EF–Tu and Phe–tRNA^{Phe} were prepared as described^{31–33}. Prior to initiation, the mRNA (GGCAAGGAGGUAAAUAUGUUCGUUACGAC; the AUG start codon coding for fMet and UUC coding for Phe are underlined) was incubated with 0.1 mM EDTA for 90 s at 80 °C and shock cooled in an ice-water bath. 70S ribosomes (3 μM) were incubated with IF1, IF2, IF3 (4.5 μM), mRNA (15 μM), and f[³H]Met–tRNA^{fMet} (7 μM) in buffer A (50 mM Tris–HCl, pH 7.5, 70 mM NH₄Cl, 30 mM KCl, 7 mM MgCl₂) containing 2 mM dithiothreitol (DTT) and 1 mM GTP for 30 min at 37 °C. Initiation efficiency was verified by nitrocellulose binding assay and radioactivity counting to be close to 100%. The complexes were purified by size-exclusion chromatography on a Biosuite 450 HR 5 μm column (Waters) using HPLC Alliance system (Waters). The cognate ternary complex EF–Tu–GTP–Phe–tRNA^{Phe} was prepared in buffer B (50 mM HEPES–KOH, pH 7.5, 70 mM NH₄Cl, 30 mM KCl, 7 mM MgCl₂, 2 mM DTT) using a twofold excess of EF–Tu over Phe–tRNA^{Phe}. Initiation complexes (0.07 μM) were mixed with excess of deacylated tRNA^{fMet} (0.2 μM) and ternary complexes (0.12 μM) in buffer C (50 mM HEPES–KOH, pH 7.5, 70 mM NH₄Cl, 30 mM KCl, 20 mM MgCl₂, 1 mM DTT, 0.6 mM spermine, 0.4 mM spermidine) in the presence of 150 μM kirromycin.

Cryo-EM analysis. Five microlitres of 0.07 μM kirromycin-stalled ribosome–EF–Tu complexes were applied onto cryo-EM grids (Quantifoil 3.5/1 μm, Jena) covered with pre-floated continuous carbon. Cryo-EM grids were prepared under controlled environmental conditions at 4 °C and 100% humidity in a vitrification device (Vitrobot Mark IV, FEI Company, Eindhoven). A total of 24,684 image frames were recorded in spot-scanning mode (4 × 4 image frames per 3.5 μm hole in the Quantifoil carbon film) on a Falcon I direct detector under liquid-nitrogen conditions with a Titan Krios electron microscope (FEI, Eindhoven) equipped with a XFEG electron source and a C_s corrector (CEOS, Heidelberg) using 300 kV acceleration voltage, an electron dose of ~40 ± 5 electrons per Å² (determination based on calibration with a Faraday cup), –0.7 to –2.5 μm defocus and a nominal magnification of 192,000×, resulting in a final pixel size of ~0.755 Å (as determined by comparing the final 3D map with atomic models from X-ray crystallography). Using the C_s corrector, electron optical aberrations were corrected to residual phase errors of 45° at scattering angles of >12 to 15 mrad (that is, less than 45° phase error at 1.8 to 2.1 Å; Extended Data Fig. 1). Linear geometrical distortions were reduced to <0.1% using the *tilt-xapole* beam coils of the C_s corrector. Furthermore, coma caused by the spot-scanning procedure was minimized using the *usimageshift* correction in the C_s corrector alignment. Ribosome particle images were extracted in a fully automated manner using template-independent custom-made software (CowPicker, B. Busche and H.S., unpublished data). The 1,603,254 extracted particle images were corrected locally for the contrast-transfer function by classification and averaging and selected according to quality of powerspectra³⁴, that is, to show Thon rings better than 3.4 Å up to 2.4 Å. In all subsequent steps, the resulting 1,339,775 contrast-transfer-function-corrected particle images were used. First, the particle images were sorted into groups of particles according to: (1) 30S body rotation, as described⁷; and (2) ligand occupancy, using supervised classification by projection matching³⁵ on the basis of a structural library of different ribosome complexes^{7,36} (Extended Data Fig. 2). Sorting in both steps was performed using low-pass-filtered reference maps and particle images binned to about 6 Å per pixel. Finally, 3D classification in RELION 1.2³⁷ was used to obtain the final set of 417,201 particle images with bound elongation factor for the refinement to high-resolution (2.9 Å) using the ‘gold-standard procedure’ in RELION 1.2³⁷ (Extended Data Fig. 3). A local resolution map computed from the two unprocessed half-maps by Resmap² revealed only few variations in local resolution over the entire ribosome complex (Fig. 1a). We obtained another cryo-EM map of a ratcheted ribosome with tRNAs in hybrid states and showing protein L31 in a distinct conformation by sorting particle images with 10° rotation angles according to ligand occupancy, as described above, resulting in a final homogeneous population of 8,073 particles, which was refined to 6.4 Å resolution (0.143 criterion) using the gold-standard procedure in RELION.

Atomic fluctuations obtained from molecular dynamics simulations. The molecular dynamics simulation of the ribosome in a pre-translocation state (pre1a) presented earlier³⁸ was extended to 2 μs. To identify the rigid core of the 50S subunit, the root mean square fluctuation (r.m.s.f.) of each atom was calculated using the program *g_rmsf* from the GROMACS simulation suite³⁹ after alignment to the 50S subunit, omitting the first 0.5 μs. The rigid core was defined as all 50S atoms excluding those of the tail of the r.m.s.f. histogram starting at the point where the frequency drops to half of the maximum frequency (0.19 nm). Finally, the r.m.s.f. of all atoms after alignment to the rigid core was calculated (Extended Data Fig. 6).

Pseudo-crystallographic refinement and model building. For initial model building, the cryo-EM density map was sharpened by applying a B factor of –120 Å², filtered to 3.1 Å resolution and masked using a pseudo bulk solvent envelope obtained by merging different versions of the cryo-EM map filtered at different frequencies

(12.0 Å, 8.0 Å, 6.0 Å and 4.0 Å) with the RAVE package⁴⁰ and Chimera⁴¹. Fourier transform of the masked cryo-EM density map to reciprocal space structure factors was performed using Crystallography and NMR System (CNS)^{42,43} employing phase significance blurring scale factors derived from FSC values in a resolution-dependent manner⁴⁴. In detail, a modified CNS input file was used for the assignment of FOMs (figure of merit) estimated based on equation (1) for the map obtained from the full data set and equation (2) for the maps obtained from two half sets:

$$\text{FOM} = \left(\frac{2 \times \text{FSC}}{(1 + \text{FSC})} \right)^{0.5} \quad (1)$$

$$\text{FOM} = (\text{FSC})^{0.5} \quad (2)$$

Obtained phase probabilities, written in the form of Hendrickson–Lattman (HL) coefficients, were used for reciprocal space refinement, performed against an MLHL target (maximum likelihood with experimental phase probability distribution) in both CNS and PHENIX⁴⁵ programs using both X-ray and electron scattering factors, respectively. Both programs employed automatic optimization of weights used to balance the relative contributions of experimental and restraints terms using a grid search. To fulfil the requirements of the crystallographic MLHL refinement, 5% of the reflections were selected randomly for the ‘Rfree’ set, which was kept identical for all refinements. Homology modelling combined with density-guided energy optimization was performed using the Rosetta package^{46,47} employing templates and alignments provided by the HHPRED server⁴⁸. Model density maps were generated based on finally refined models, without bulk solvent correction as implemented in PHENIX. Map normalization (mean and standard deviation of density values are 0 and 1.0, respectively) was performed using MAPMAN (Rave package).

The initial fit of an atomic model of the *E. coli* ribosome assembled from various crystal structures (PDB codes: 4GD2⁴⁹ (30S)⁴⁹, 3R8T (50S)⁴⁹, 2J00 (mRNA, tRNA^{fMet})⁵⁰, 3L0U (tRNA^{Phe})⁵¹, 1OB2 (EF–Tu) (R. C. Nielsen *et al.* unpublished data)) was performed using Chimera, followed by rigid body refinement in the PHENIX program. The atomic model was refined with deformable elastic network (DEN) restraints⁵² in CNS with alternating cycles of manual rebuilding in Coot⁵³ and monitoring the local fit to the density with RESOLVE⁵⁴. In addition the overall refinement progress was monitored by calculating CC_{work} and CC_{free} (ref. 8), as well as the correlation between the cryo-EM and the model map (FSC_{work}). The one-dimensional structure factor derived by rotational averaging from the initially refined model was used to re-sharpen the raw cryo-EM density map. Prior to Fourier transformation, the re-sharpened, normalized 3D cryo-EM map was solvent flattened using a smoothed model-based envelope (Rave package, Chimera), encompassing the volume within the distance of at least 3.0 Å from each atom. As the density in the protein region is not supposed to be negative, voxels with negative density in the protein region were set to zero during the solvent flattening process by the MAPMASK program in the CCP4 suite⁵⁵. Further model improvement and fitting were facilitated by real space refinement (ERRASER⁵⁶ and phenix.real_space_refine⁵⁷ against the map calculated using the working set of reflections only) and manual corrections in Coot combined with reciprocal space refinement. Modelling of post-transcriptional modifications was performed in Coot and was based on thorough analysis of the cryo-EM map. Modifications resulting from addition or substitution of an atom or atoms in comparison with unmodified bases were modelled if the presence of additional atoms or consequent changes in shape (for dihydrouridine) were supported by the cryo-EM map. Pseudouridines were modelled as indicated by additional polar/hydrogen-bond interactions formed by the additional amine group. For one methylation (m⁵747 in 23S rRNA) showing no well-defined corresponding density and two pseudouridines (Ψ746 and Ψ2457 in 23S rRNA) with no clear additional interactions, modifications were modelled on the basis of ref. 11 and references therein. In all other cases manual modelling of modified nucleotides was performed only if the cryo-EM map was well defined. New stereochemistry definitions for non-standard ligands were generated with phenix.reel. A homology model of protein L31 was built in Rosetta using the *T. thermophilus* X-ray structure (PDB ID: 3I8I)⁵⁸ and constraints from the present cryo-EM map filtered to 4.5 Å resolution. Models of protein L9 and L31 were manually adjusted to fit the cryo-EM map filtered at 3.9 Å and 4.5 Å resolution, respectively in the programs O (ref. 59) and Coot. The models were further refined in real space using Rosetta followed by phenix.real_space_refine against the map created from working set reflections only. To maintain the intermolecular interactions of L9 and L31 proteins, the atomic models used for real space refinement in phenix.real_space_refine included surrounding proteins and parts of RNA chains within a radius of at least 10 Å. Improved protein models were included in the overall model used for the final reciprocal space refinement against 2.9 Å resolution data generated from the sharpened and solvent-flattened 3D cryo-EM map in PHENIX. The final model consisting of 152,718 individual atoms has been refined to 24.08% and 0.922 for R_{work} and CC_{work} (definition is given below), respectively. The final model exhibits a good stereochemistry

with 85.59% of residues in the most favoured region and 3.30% residues in the disallowed region of the Ramachandran plot, protein side chain outliers of 2.63% and all atom clash score 9.15. Detailed refinement statistics are presented in Extended Data Table 1. The model for another conformer of protein L31 found in a cryo-EM map of the ribosome in complex with two tRNAs in hybrid states was built at 6.5 Å resolution, as described above for L9 and L31.

Refinement of half maps. Refinement of the final model against data sets obtained from two half maps was performed at a resolution of 2.9 Å in PHENIX using five to seven cycles of combined positional (real and reciprocal space) and atomic displacement parameter (ADP) refinement combined with automatically identified TLS (translation/libration/screw) groups. To remove possible model bias from the model refined against reflections obtained from the reconstruction using all the particles, a similar strategy was used as for higher-resolution refinements (a 0.5 Å random shift and additional restraints), as described below. The FSC and CC were calculated between the model and the half map used for refinement, as well as between the model and the other half map for cross-validation (Extended Data Fig. 3b).

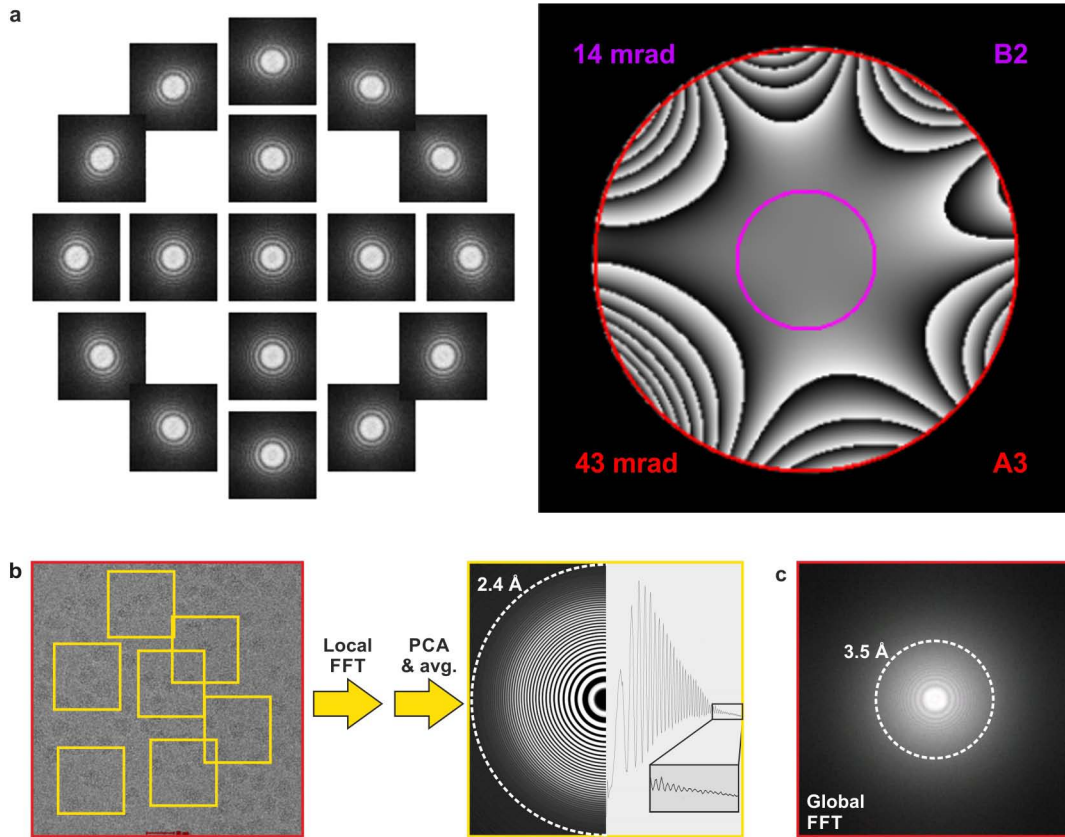
Higher-resolution refinements. The final atomic model of the *E. coli* ribosome was divided into three sub-models containing about 65%, 43% and 24% of all residues, respectively, with each sub-model exhibiting similar B factors and resolution estimates for the corresponding fragment of the cryo-EM map (Extended Data Fig. 3). The resulting three models were used to calculate smoothed masks encompassing the volume within a distance of at least 2.5 Å from each atom. Those masks were used to cut the required portion of the cryo-EM density map using a pseudo bulk solvent flattening procedure before conversion to reciprocal space structure factors, as described above. Phase significance blurring scale factors applied during the Fourier transform were derived from FSC values calculated between fragments of the two half maps masked by model-based envelopes. The refinement of individual models (initially to 2.75 Å, 2.60 Å and 2.50 Å for 65%, 43% and 24% of all residues, respectively) against MLHL targets were performed in PHENIX by gradually decreasing the high-resolution limit in 0.05 Å steps, for example, local resolution refinements starting with 2.50 Å were performed at 2.50 Å, 2.55 Å, 2.60 Å, 2.65 Å, 2.70 Å and 2.75 Å. To eliminate possible bias against the model refined at 2.9 Å resolution, the atoms were displaced by a random translation up to 0.1 Å before performing the full refinement using restraints for secondary structure, base-pairing, base-planarity and hydrogen bonding. The pseudo crystallographic high-resolution limit was selected based on several criteria: (1) the overall R and R_{work} factors (lower than 1/10 of the highest resolution limit); (2) the Pearson correlation coefficient calculated between F_{model} and F_{EM} (CC_{work}) used for refinement should be greater than 0.2 for the highest resolution shell and the overall correlation coefficient (CC_{overall}) should not be lower than 0.9; (3) the calculated FSC_{work} value between model map coefficients ($F_{\text{model}}, \text{phase}_{\text{model}}$) and structure factors derived from the cryo-EM map ($F_{\text{EM}}, \text{phase}_{\text{EM}}$) used for refinement should be greater than 0.5 for the highest resolution shell; (4) the calculated crystallographic R factor for the highest resolution shell should be not greater than 51%. The mentioned statistical values have been calculated in a resolution-dependent manner using PHENIX and SFALL (CCP4 suite) for 20 shells comprising a similar number of reflections (default number of shells for reporting refinement statistics in PHENIX).

Preparation of figures. Figures were generated using Pymol 1.7 (Schrodinger, LLC.), UCSF CHIMERA 1.9⁴¹, AMIRA 5.2.2 (Visage Imaging, Richmond VIC) and PRISM 5 (GraphPad Software, La Jolla).

31. Milon, P. *et al.* Transient kinetics, fluorescence, and FRET in studies of initiation of translation in bacteria. *Methods Enzymol.* **430**, 1–30 (2007).
32. Rodnina, M. V. *et al.* Thiostrepton inhibits the turnover but not the GTPase of elongation factor G on the ribosome. *Proc. Natl Acad. Sci. USA* **96**, 9586–9590 (1999).
33. Rodnina, M. V. & Wintermeyer, W. GTP consumption of elongation factor Tu during translation of heteropolymeric messenger-RNAs. *Proc. Natl Acad. Sci. USA* **92**, 1945–1949 (1995).
34. Sander, B., Golas, M. M. & Stark, H. Automatic CTF correction for single particles based upon multivariate statistical analysis of individual power spectra. *J. Struct. Biol.* **142**, 392–401 (2003).
35. Valle, M. *et al.* Cryo-EM reveals an active role for aminoacyl-tRNA in the accommodation process. *EMBO J.* **21**, 3557–3567 (2002).
36. Stark, H. *et al.* Ribosome interactions of aminoacyl-tRNA and elongation factor Tu in the codon-recognition complex. *Nature Struct. Mol. Biol.* **9**, 849–854 (2002).
37. Scheres, S. H. W. RELION: Implementation of a Bayesian approach to cryo-EM structure determination. *J. Struct. Biol.* **180**, 519–530 (2012).
38. Bock, L. V. *et al.* Energy barriers and driving forces in tRNA translocation through the ribosome. *Nature Struct. Mol. Biol.* **20**, 1390–1396 (2013).
39. Pronk, S. *et al.* GROMACS 4.5: a high-throughput and highly parallel open source molecular simulation toolkit. *Bioinformatics* **29**, 845–854 (2013).
40. Kleywegt, G. J. & Jones, T. A. Software for handling macromolecular envelopes. *Acta Crystallogr. D* **55**, 941–944 (1999).
41. Pettersen, E. F. *et al.* UCSF Chimera—a visualization system for exploratory research and analysis. *J. Comput. Chem.* **25**, 1605–1612 (2004).

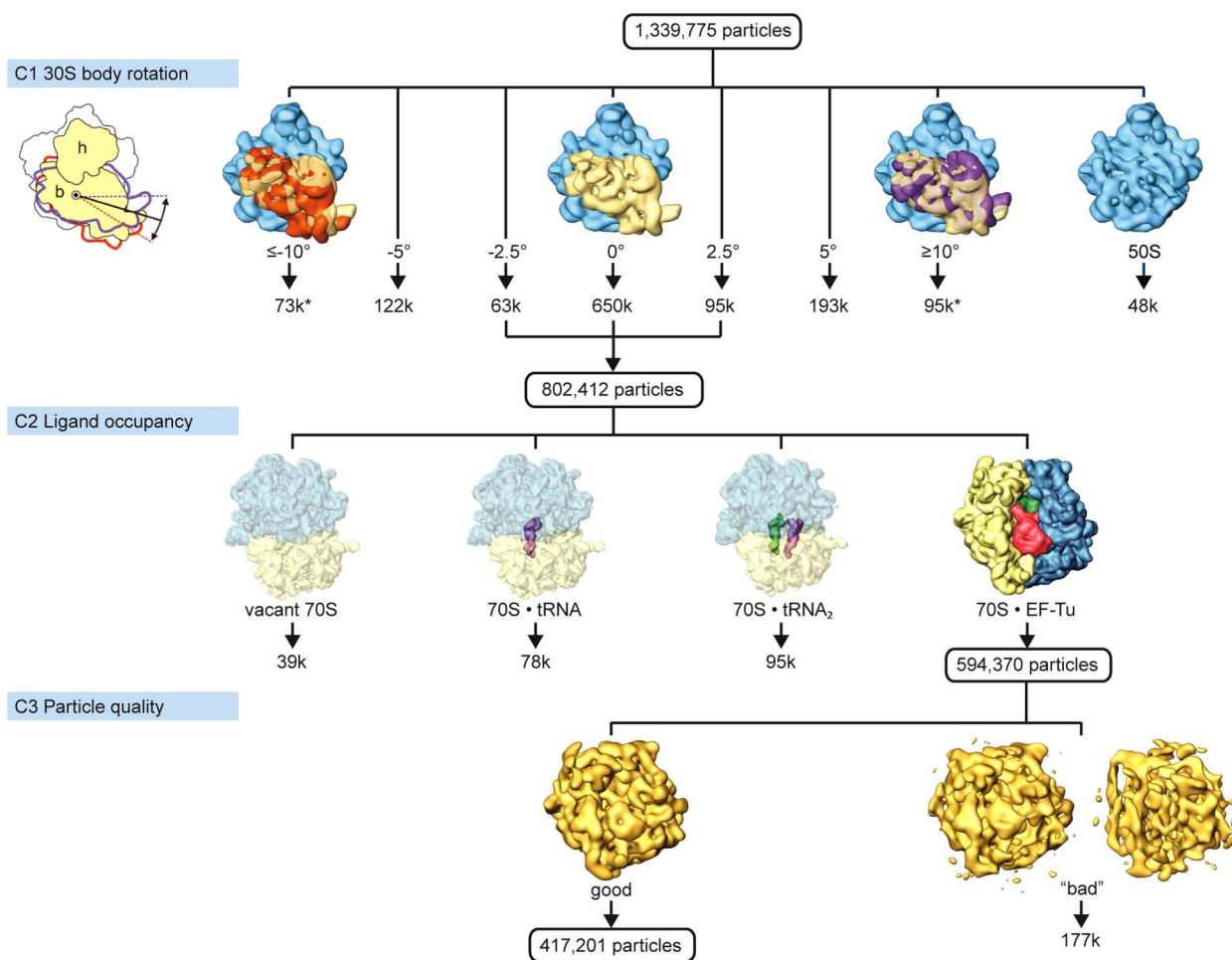
42. Brunger, A. T. Version 1.2 of the Crystallography and NMR system. *Nature Protocols* **2**, 2728–2733 (2007).
43. Brünger, A. T. *et al.* Crystallography & NMR system: a new software suite for macromolecular structure determination. *Acta Crystallogr. D* **54**, 905–921 (1998).
44. Greber, B. J. *et al.* The complete structure of the large subunit of the mammalian mitochondrial ribosome. *Nature* **515**, 283–286 (2014).
45. Adams, P. D. *et al.* PHENIX: a comprehensive Python-based system for macromolecular structure solution. *Acta Crystallogr. D Biol. Crystallogr.* **66**, 213–221 (2010).
46. DiMaio, F. *et al.* Improved molecular replacement by density- and energy-guided protein structure optimization. *Nature* **473**, 540–543 (2011).
47. DiMaio, F., Tyka, M. D., Baker, M. L., Chiu, W. & Baker, D. Refinement of protein structures into low-resolution density maps using rosetta. *J. Mol. Biol.* **392**, 181–190 (2009).
48. Söding, J., Biegert, A. & Lupas, A. N. The HHpred interactive server for protein homology detection and structure prediction. *Nucleic Acids Res.* **33**, W244–W248 (2005).
49. Dunkle, J. A. *et al.* Structures of the bacterial ribosome in classical and hybrid states of tRNA binding. *Science* **332**, 981–984 (2011).
50. Selmer, M. *et al.* Structure of the 70S ribosome complexed with mRNA and tRNA. *Science* **313**, 1935–1942 (2006).
51. Byrne, R. T., Konevega, A. L., Rodnina, M. V. & Antson, A. A. The crystal structure of unmodified tRNA^{Phe} from *Escherichia coli*. *Nucleic Acids Res.* **38**, 4154–4162 (2010).
52. Schröder, G. F., Levitt, M. & Brunger, A. T. Super-resolution biomolecular crystallography with low-resolution data. *Nature* **464**, 1218–1222 (2010).
53. Emsley, P., Lohkamp, B., Scott, W. & Cowtan, K. Features and development of Coot. *Acta Crystallogr. D* **66**, 486–501 (2010).
54. Terwilliger, T. C. Maximum-likelihood density modification. *Acta Crystallogr. D* **56**, 965–972 (2000).
55. The CCP4 Suite: programs for protein crystallography. *Acta Crystallogr. D* **50**, 760–763 (1994).
56. Chou, F.-C., Sripakdeevong, P., Dibrov, S. M., Hermann, T. & Das, R. Correcting pervasive errors in RNA crystallography through enumerative structure prediction. *Nature Methods* **10**, 74–76 (2013).
57. Afonine, P. V., Headd, J. J., Terwilliger, T. C. & Adams, P. D. New tool: phenix.real_space_refine. *Computational Crystallography Newsletter* **4**, 43–44 (2013).
58. Jenner, L., Demeshkina, N., Yusupova, G. & Yusupov, M. Structural rearrangements of the ribosome at the tRNA proofreading step. *Nature Struct. Mol. Biol.* **17**, 1072–1078 (2010).
59. Jones, T. A. & Kjeldgaard, M. Electron-density map interpretation. *Methods Enzymol.* **277**, 173–208 (1997).
60. Allegretti, M., Mills, D. J., McMullan, G., Kühlbrandt, W. & Vonck, J. Atomic model of the F420-reducing [NiFe] hydrogenase by electron cryo-microscopy using a direct electron detector. *eLife* **3**, e01963 (2014).
61. Bartesaghi, A., Matthies, D., Banerjee, S., Merk, A. & Subramaniam, S. Structure of β -galactosidase at 3.2-Å resolution obtained by cryo-electron microscopy. *Proc. Natl Acad. Sci. USA* **111**, 11709–11714 (2014).
62. Burmeister, W. P. Structural changes in a cryo-cooled protein crystal owing to radiation damage. *Acta Crystallogr. D* **56**, 328–341 (2000).
63. Rosenthal, P. B. & Henderson, R. Optimal determination of particle orientation, absolute hand, and contrast loss in single-particle electron cryomicroscopy. *J. Mol. Biol.* **333**, 721–745 (2003).
64. Grosse-Kunstleve, R. W., Sauter, N. K., Moriarty, N. W. & Adams, P. D. The Computational Crystallography Toolbox: crystallographic algorithms in a reusable software framework. *J. Appl. Crystallogr.* **35**, 126–136 (2002).
65. Demirci, H. *et al.* Modification of 16S ribosomal RNA by the KsgA methyltransferase restructures the 30S subunit to optimize ribosome function. *RNA* **16**, 2319–2324 (2010).
66. Helsler, T. L., Davies, J. E. & Dahlberg, J. E. Mechanism of kasugamycin resistance in *Escherichia coli*. *Nature* **235**, 6–9 (1972).
67. O'Connor, M., Thomas, C. L., Zimmermann, R. A. & Dahlberg, A. E. Decoding fidelity at the ribosomal A and P sites: influence of mutations in three different regions of the decoding domain in 16S rRNA. *Nucleic Acids Res.* **25**, 1185–1193 (1997).
68. François, B. *et al.* Crystal structures of complexes between aminoglycosides and decoding A site oligonucleotides: role of the number of rings and positive charges in the specific binding leading to miscoding. *Nucleic Acids Res.* **33**, 5677–5690 (2005).
69. Jiang, J., Aduri, R., Chow, C. S. & SantaLucia, J. Structure modulation of helix 69 from *Escherichia coli* 23S ribosomal RNA by pseudouridylations. *Nucleic Acids Res.* **42**, 3971–3981 (2013).
70. Davis, D. R. Stabilization of RNA stacking by pseudouridine. *Nucleic Acids Res.* **23**, 5020–5026 (1995).
71. Ortiz-Meoz, R. F. & Green, R. Helix 69 is key for uniformity during substrate selection on the ribosome. *J. Biol. Chem.* **286**, 25604–25610 (2011).
72. Seidelt, B. *et al.* Structural insight into nascent polypeptide chain-mediated translational stalling. *Science* **326**, 1412–1415 (2009).
73. Pulk, A. & Cate, J. H. Control of ribosomal subunit rotation by elongation factor G. *Science* **340**, 1235970 (2013).
74. Vorstenbosch, E., Pape, T., Rodnina, M., Kraal, B. & Wintermeyer, W. The G222D mutation in elongation factor Tu inhibits the codon-induced conformational changes leading to GTPase activation on the ribosome. *EMBO J.* **15**, 6766–6774 (1996).
75. Daviter, T., Wieden, H.-J. & Rodnina, M. V. Essential role of histidine 84 in elongation factor Tu for the chemical step of GTP hydrolysis on the ribosome. *J. Mol. Biol.* **332**, 689–699 (2003).

76. Voorhees, R. M., Schmeing, T. M., Kelley, A. C. & Ramakrishnan, V. The mechanism for activation of GTP hydrolysis on the ribosome. *Science* **330**, 835–838 (2010).
77. Pintilie, G. D., Zhang, J., Goddard, T. D., Chiu, W. & Gossard, D. C. Quantitative analysis of cryo-EM density map segmentation by watershed and scale-space filtering, and fitting of structures by alignment to regions. *J. Struct. Biol.* **170**, 427–438 (2010).
78. Selmer, M., Gao, Y.-G., Weixlbaumer, A. & Ramakrishnan, V. Ribosome engineering to promote new crystal forms. *Acta Crystallogr. D* **68**, 578–583 (2012).



Extended Data Figure 1 | Aberration-corrected cryo-EM. **a**, Exemplary Zemlin tableau (left) and phase diagram (right) as obtained for the present data set with the CEOS software by correcting electron optical aberrations using the C_s corrector. The resulting phase errors were less than 45° at $\leq 2.1 \text{ \AA}$ (that is, at scattering angles of 12 to 15 mrad) over up to 36 h of image acquisition. The main limiting aberration is axial coma (B2) and the next limiting aberration would be threefold astigmatism (A3). **b**, Local correction for the contrast transfer function. From micrographs (left) areas with individual ribosome

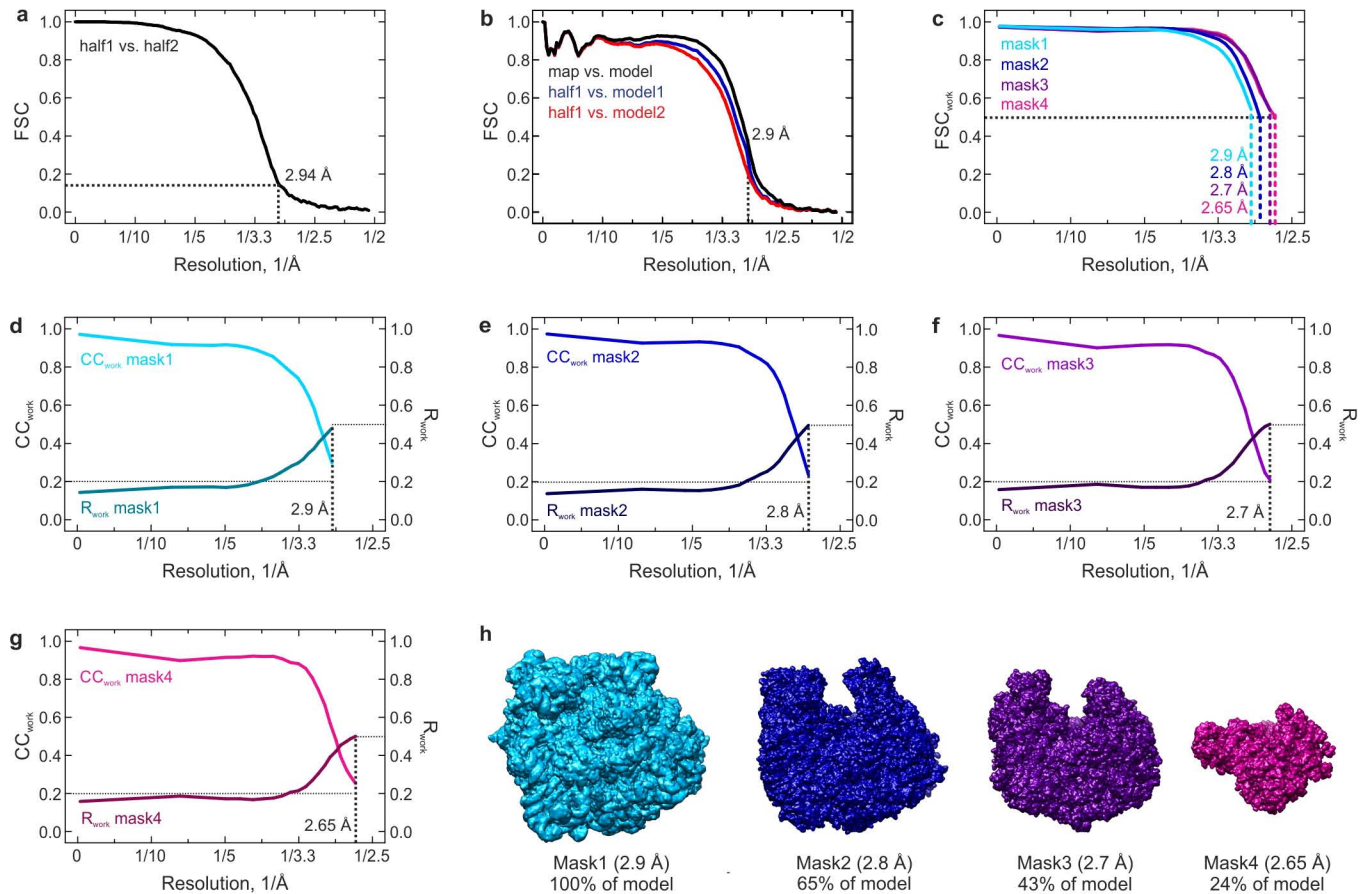
particles (yellow frames) were extracted and local power spectra were computed for each of these areas by fast Fourier transform algorithms (FFT). Local power spectra were subjected to principal component analysis (PCA) and classification to average power spectra with similar contrast transfer function parameters that were obtained from different micrographs. Class averages of power spectra reveal an improved signal-to-noise ratio in Thon rings which are clearly visible up to 2.4 Å (right). **c**, Global power spectrum from a single micrograph showing Thon rings up to 3.5 Å.



Extended Data Figure 2 | Hierarchical sorting of ribosome particle images.

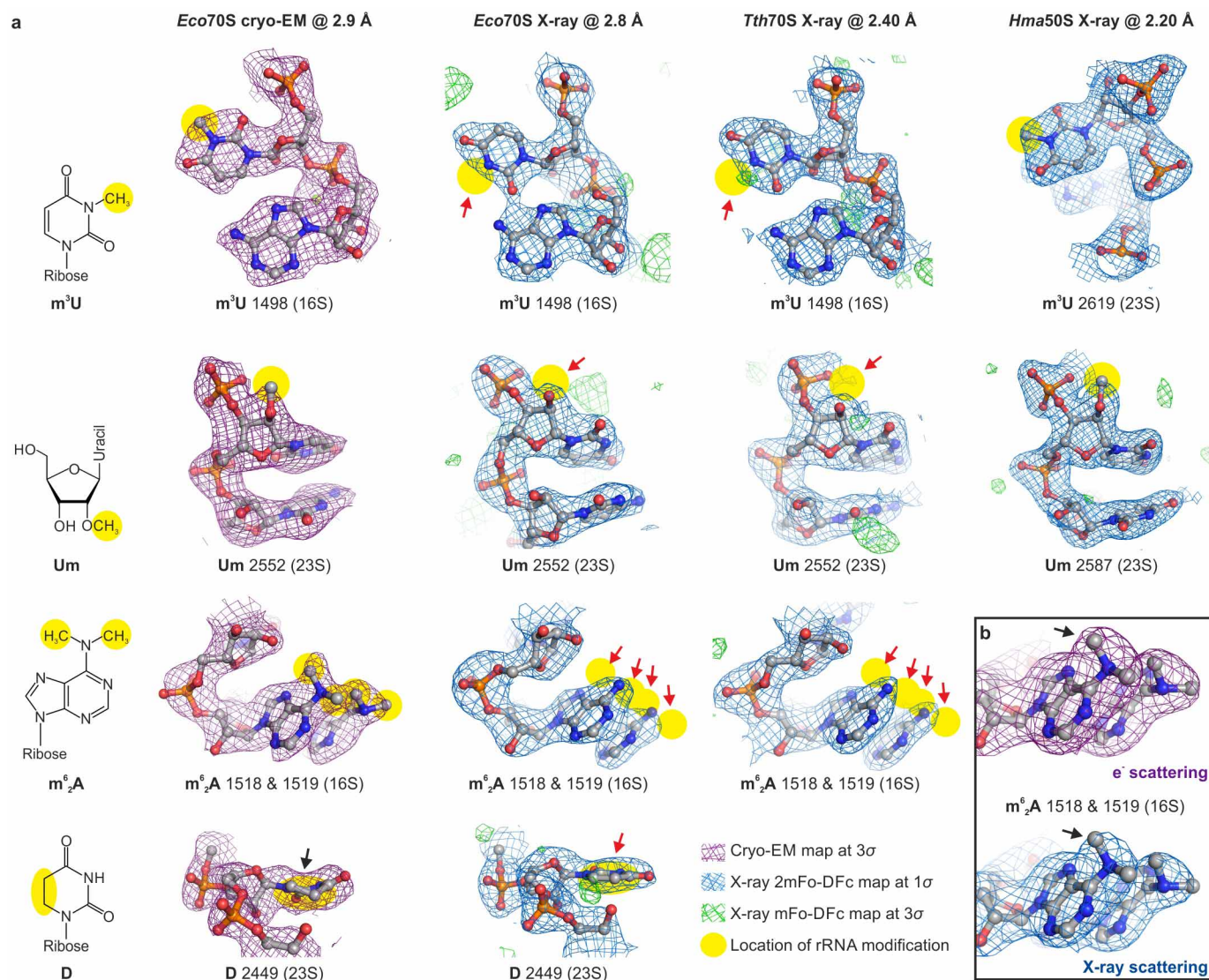
Ribosome particles were sorted in three steps according to: (1) global ribosome conformation (C1), that is, 30S body rotation⁷; and (2) ligand occupancy (C2)³⁵ and particle quality (C3)³⁷ (Methods). The asterisk denotes

particles assigned to the largest 30S body rotations $\leq -10^\circ$ and $\geq 10^\circ$ which contain particles with extreme 30S rotation angles, but also low-quality particle images.



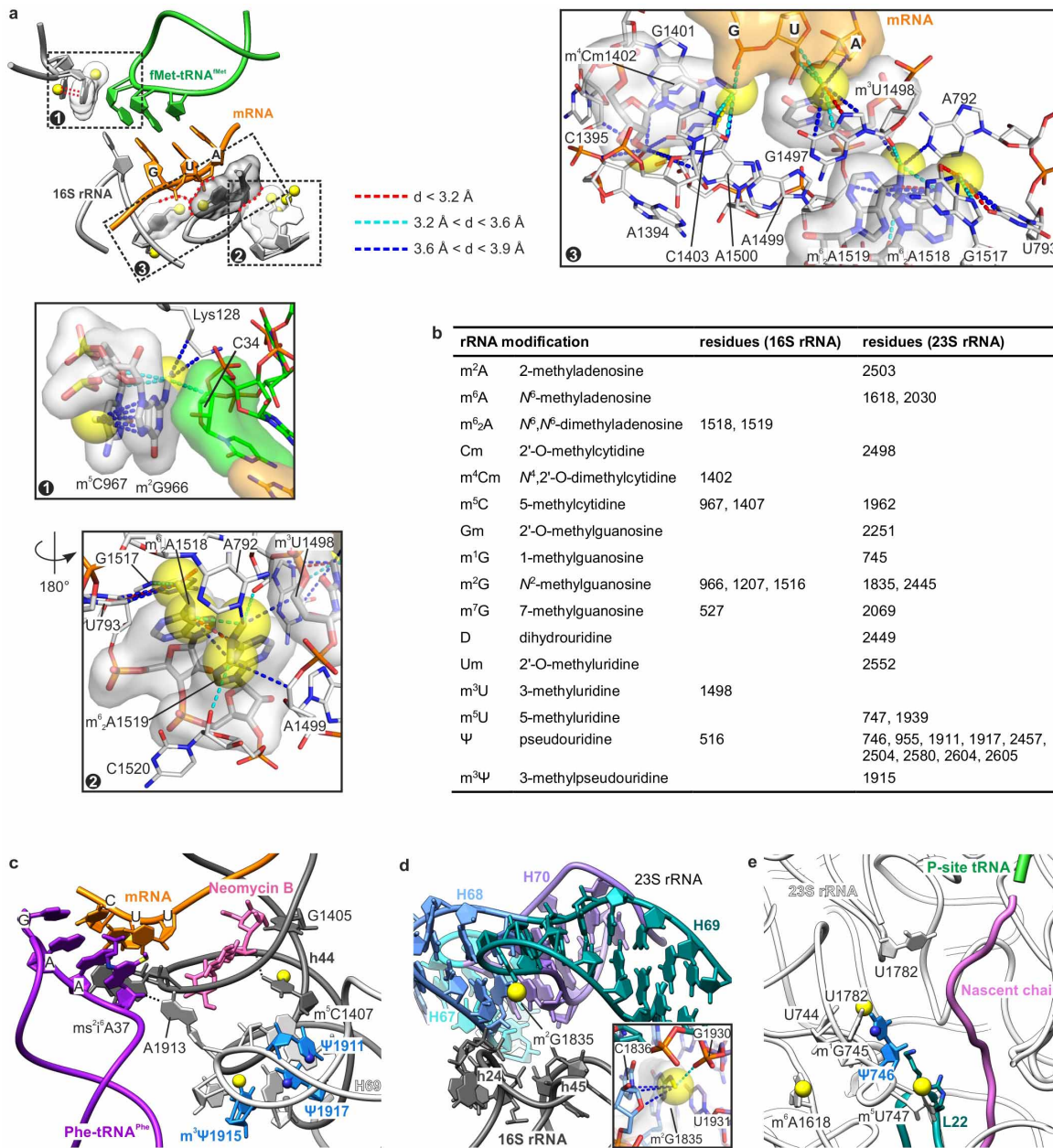
Extended Data Figure 3 | Resolution curves and model validation of the *E. coli* 70S ribosome-EF-Tu cryo-EM structure. **a**, Fourier-shell correlation (FSC) curve (black) for the 70S ribosome cryo-EM reconstruction computed between the masked independent half-maps (half1 and half2) that were obtained by so-called 'gold-standard' refinement in RELION³⁷. The resolution of the cryo-EM reconstruction is ~ 2.9 Å according to the 0.143 criterion⁶³ (black dashed line). **b**, FSC curves computed between cryo-EM maps and model maps generated from refined atomic coordinates. The vertical black dashed line indicates the maximum resolution at which the full atomic models were refined. Black, the FSC curve between the final cryo-EM map (map) and the final model (model); blue, the FSC curve between half map 1 (half1) and the model obtained by refinement only against half map 1 (model1); red, the FSC curve between half map 1 and the model obtained by refinement only against half map 2 (model2). **c**, FSC curves (FSC_{work}) between reflections from

solvent-flattened cryo-EM map and model as obtained by pseudo-crystallographic refinement of the complete ribosome model (mask1) and three sub-models using different masks corresponding to local variations in resolution (mask2–4; Methods) as shown in **h**. Coloured numbers indicate the highest resolution used in refinement with the respective mask as indicated by the colour code. For all refinements, the FSC is above the 0.5 threshold (black dashed line) in the highest-resolution shell. Differences to **b** result largely from solvent-flattening before Fourier transformation for refinement (Methods). **d–g**, CC_{work} and R_{work} as obtained by refinement using the respective mask (see labels). For a reliable resolution estimate CC_{work} (ref. 8) is expected to be >0.2 and $R_{work} < 0.51$ in the highest-resolution shell. **h**, Isosurface representations of the mask used for local refinements; '%' indicates the fraction of atoms of the complete model entailed in the refinement with the respective mask.



Extended Data Figure 4 | Modifications in rRNA. Comparison between cryo-EM and X-ray crystallography. **a**, Experimental densities. In each row density maps for the same type of rRNA modification are shown (from left to right): for the present cryo-EM map and for the current best resolved bacterial and archaeal ribosome maps determined by X-ray crystallography, that is, the bacterial 70S ribosome from *E. coli* (*Eco*70S) at 2.8 Å resolution⁵ (PDB IDs: 4TPA and 4TPB); the bacterial 70S ribosome from *T. thermophilus* (*Tth*70S) at 2.4 Å resolution⁹ (PDB IDs: 4RB5 and 4RB6); and the archaeal 50S subunit from *Haloarcula marismortui* (*Hma*70S) at 2.2 Å resolution¹⁰ (PDB ID: 1VQ0). *E. coli* numbering is used for bacterial ribosome structures. Locations of rRNA modifications as determined by biochemical data are marked by yellow circles, modifications not observed in the density maps are

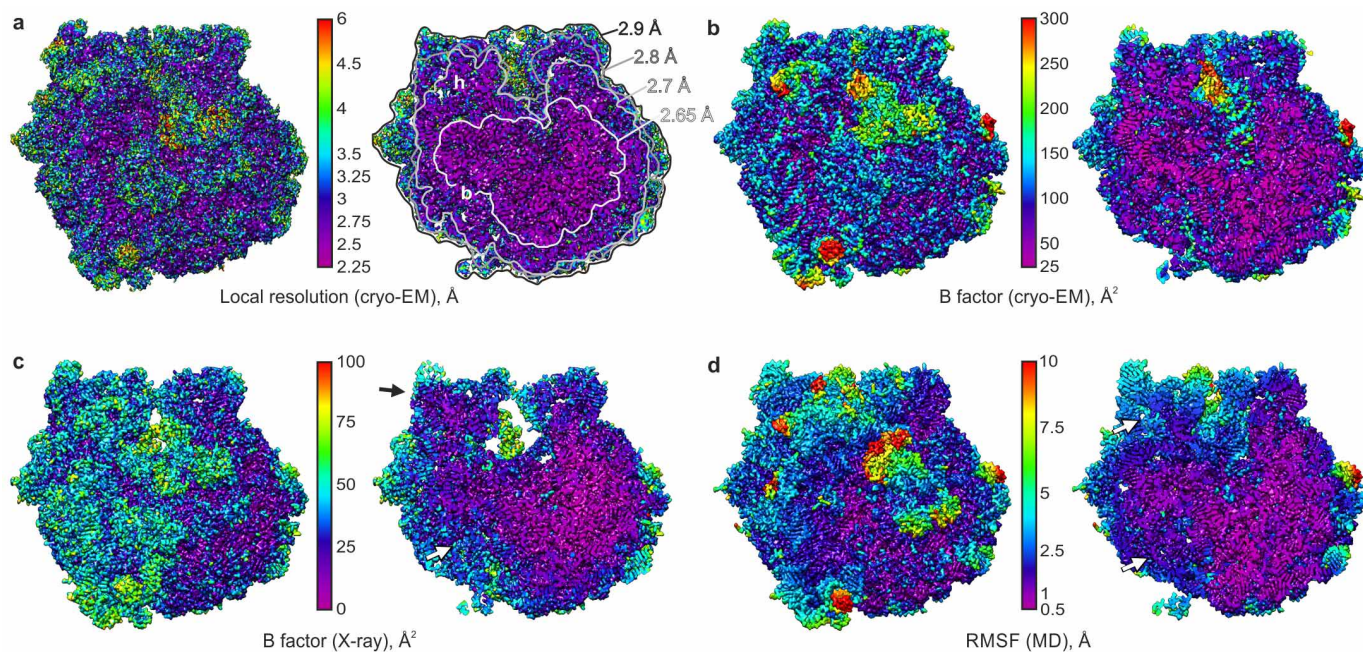
denoted by red arrows and the black arrow designates the non-planarity of dihydrouridine observed in the cryo-EM map. **b**, Model-based densities for m^2A 1518 and m^2A 1519 showing slight differences due to scattering properties. Densities were computed in CCTBX⁶⁴ at 2.65 Å resolution from our final model with atomic-displacement factors kept unchanged using electron (e^- scattering, purple) and X-ray scattering factors (X-ray scattering, blue), respectively. Map thresholds were normalized to show similar density levels for the electron-rich phosphate groups. Accordingly, the absence of densities for modifications in crystallographic maps also at higher resolutions may result from differences in electron and X-ray scattering and in data quality which is affected, for example, by local and global disorder.



Extended Data Figure 5 | rRNA modifications in the *E. coli* 70S ribosome.

a, Stabilizing effects of 16S rRNA methyl groups in the P site of the decoding centre. Numbers in the overview (top left) mark the positions of close-ups (1–3), which show the interactions of the rRNA methyl groups with distances colour-encoded by dashed lines. Close-up 1: Stacking network of m⁵C966 and m⁵C967 stabilizing binding of initiator tRNA. Close-ups 2, 3: rRNA modifications impacting mRNA binding. The universally conserved bulky dimethylamine groups of m^{6,2}A1518 and m^{6,2}A1519 stabilize their direct environment by steric encumbrance explaining their requirement for correct packing of 16S rRNA helices 24a, 44 and 45⁶⁵. In particular, the dimethylamine of m^{6,2}A1519 is involved in medium and long-range repulsive interactions with the backbone of m³U1498 and the 2' O of C1520, while its conformation is mostly determined by the dimethylamine moiety of the adjacent m²A1518 which, in turn, is fixed by short repulsive interactions with O6 of G1517 and O4 of U793. The additional methyl groups of m^{6,2}A1519 interact with A792, which provides part of the binding site for the antibiotic kasugamycin¹⁵, accounting for the resistance against kasugamycin upon demethylation of m^{6,2}A1519⁶⁶. Furthermore, m^{6,2}A1518 and m^{6,2}A1519 impact initiation⁶⁷ possibly via m³U1498 whose backbone interacts with m^{6,2}A1519, while its modified base contacts the mRNA backbone. The methyl groups of m³U1498 and m⁴Cm1402 form part of the binding site for the initiation codon and modulate translation initiation^{13,14} by steric encumbrance and/or by preventing

direct hydrogen bonds with the mRNA backbone. **b**, Constitutive rRNA modifications in the *E. coli* 70S ribosome (list adapted from ref. 11 and references therein). **c**, rRNA modifications in the A site of the decoding centre and helix 69 of 23S rRNA (H69). The binding site of aminoglycosides in helix 44 of 16S rRNA (h44)—including N4 of m⁵C1407—is indicated for neomycin B (magenta, superposition from PDB ID: 2ET4)⁶⁸. The three pseudouridines stabilizing H69⁶⁹ by enhancing base stacking⁷⁰ are depicted in blue. The methyl group (yellow) on m³Ψ1917 in H69 prevents potential base-pairing with A1913, a residue important for uniform tRNA selection⁷¹. Note the flipped out conformation of A1913 facilitating interaction with the 2' OH of m²s⁶iA37 of the distorted Phe-tRNA^{Phe} (purple), which, in turn, stacks onto A36 of the tRNA anticodon. **d**, Methyl group on m²G1835 of 23S rRNA enhancing subunit association. The four helices of 23S rRNA that intersect around residue m²G1835 and form intersubunit bridges B2b and B2c with helices 24 (h24) and 45 (h45) of 16S rRNA (dark grey) are denoted in different colours: helix 67 (H67), light blue; helix 68 (H68), blue; helix 69 (H69), teal; helix 70 (H70), purple. Inset, contacts of the methyl group on m²G1835 with adjacent residues which, in turn, interact with 16S rRNA. **e**, Cluster of 23S rRNA modifications in the peptide exit tunnel. The modified rRNA residues, the functionally important nearby tip of protein L22 (teal), P-site fMet-tRNA^{fMet} (green) and a model of the nascent peptide chain (pink, superposition from PDB ID: 2WWL)⁷² are indicated.



Extended Data Figure 6 | Visualization of structural dynamics of the ribosome by different approaches. **a–d.** In each panel, the ribosome is shown from the factor binding site on the left and in cut-away view on the right; h denotes the head and b the body of the 30S ribosomal subunit. **a.** Present cryo-EM map coloured according to local resolution as determined by Resmap². **b.** Present cryo-EM map coloured according to the B factors obtained from the pseudo-crystallographic atomic model refinement (Methods). **c.** Model map of the 2.95 Å crystal structure of the *E. coli* 70S ribosome⁷³ (PDB IDs: 4KJ1 and 4KJ2) coloured according to respective B factors. The black

arrow denotes the stabilization of the 30S head region by crystal contacts, whereas the 30S body (white arrow) is less constrained by crystal contacts and shows higher B factors, indicating larger flexibility for this region. **d.** Snapshot from molecular dynamics trajectory of the *E. coli* 70S ribosome coloured according to root mean squared fluctuations (RMSFs) obtained from the full 2 μ s explicit solvent molecular dynamics simulation (Methods). Note the large fluctuations of the 30S head and body (white arrows) of the ribosome in solution not constrained by crystal contacts.

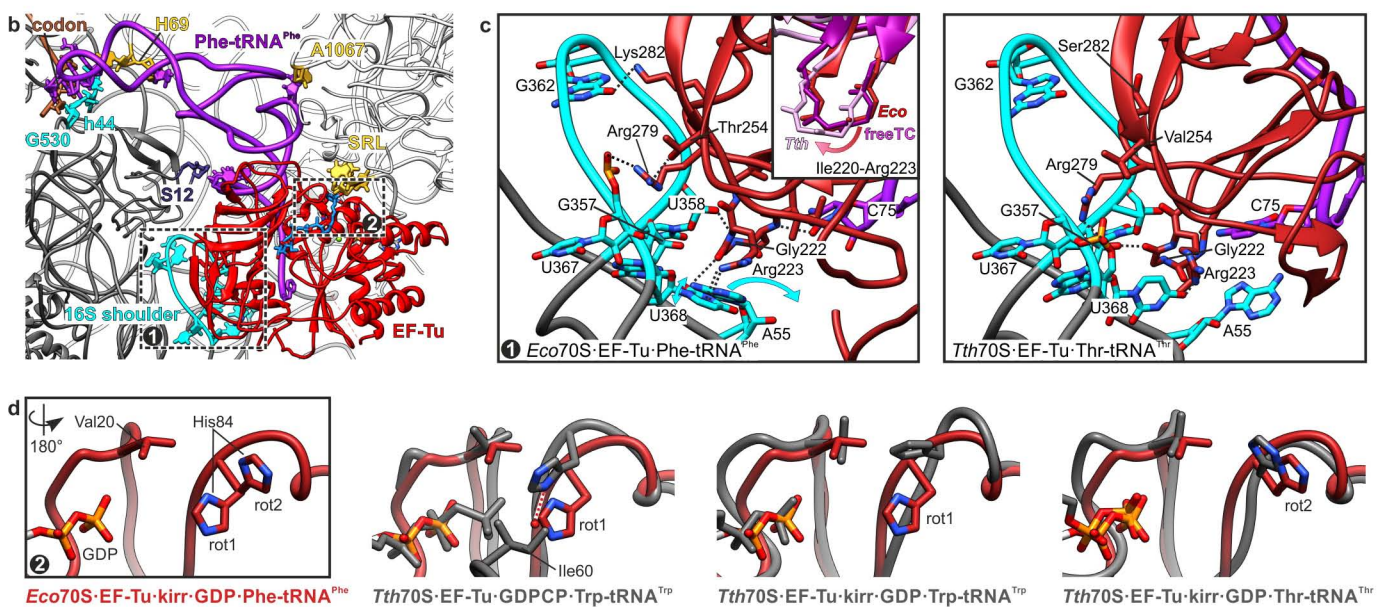
a Differences in tRNA conformation and tRNA-ribosome interactions*

complex	tRNA ^{Phe†}	70S-EF-Tu-Phe-tRNA ^{Phe}	70S-EF-Tu-Thr-tRNA ^{Thr}	70S-EF-Tu-Trp-tRNA ^{Trp}
organism/PDB ID	<i>E. coli</i> /3L0U	<i>E. coli</i> /present model	<i>T. thermophilus</i> /2WRN,2WRO	<i>T. thermophilus</i> /2Y18,2Y19
tRNA structure				
G10:C25:G44	base triple	base triple	base pair	base triple
A26:U45	none	WC	none (G:G)	WC
G27:C43	WC	WC	none (C:G)	WC (C:G)
G15:C48	reverse WC	reverse WC	none	none (A:U)
D16:U59	D:U‡	none	none (D:A)	none (D:G)
G1:C72	WC	WC	none, C72 flipped out	WC
tRNA-23S rRNA interactions				
C56-A1067	n.a.	parallel base-stacking	ribose-base stacking	T-shaped base-stacking
D20-U1066	n.a.	none	H-bonding distance	none
tRNA-16S rRNA interactions				
C75-A55	n.a.	none (A55 flipped in)	stacking (A55 flipped out)	none (A55 flipped in)

*abbreviations: WC, Watson-Crick base pair; none, no base pairing or no interaction; n.a., not applicable

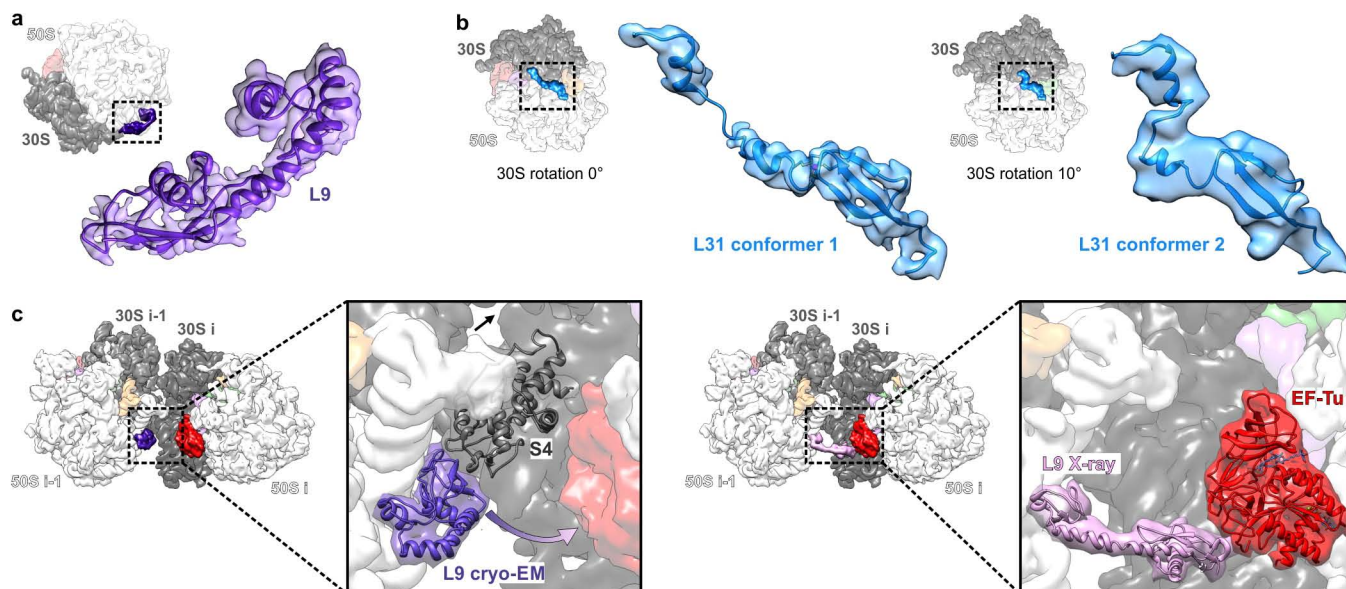
†unmodified; free modified tRNA^{Phe} from *E. coli* not available

‡base pair in modified tRNA^{Phe} from *Saccharomyces cerevisiae* (PDB ID 1EHZ)



Extended Data Figure 7 | Structure of *E. coli* EF-Tu-Phe-tRNA^{Phe} bound to the ribosome. a, Detailed comparison of the distorted A/T-site-tRNA interactions between the *E. coli* and *T. thermophilus* ribosome-EF-Tu-kirromycin complexes^{6,26} and the free *E. coli* tRNA^{Phe51}. We found significant differences in tRNA conformation and interactions implicated in the GTPase activation mechanism²⁶ that correlate with ribosome binding and differences in organism and tRNA species. Here and below residue numbers refer to *E. coli*. b, Overview of the *E. coli* ribosome-EF-Tu structure. The residues interacting with the EF-Tu ternary complex (depicted in stick representation) generally agree with those seen in the *T. thermophilus* structures^{6,26}. rRNA helices are denoted as: h44, helix 44 of 16S rRNA; H69, helix 69; and SRL, sarcin-ricin loop of 23S rRNA. The dashed boxes indicate the parts of the structure magnified in c and d. c, Structural differences in an important ribosome-EF-Tu interaction. In the *E. coli* structure (*Eco*, left panel) residues A55 and A368 of 16S rRNA assume different conformations (cyan arrows) and interact differently with the ribosome and EF-Tu-tRNA complex

than in the *T. thermophilus* structure (*Tth*, right panel, PDB ID: 2WRN)²⁶. Furthermore, the differences in EF-Tu sequence result in slightly different ribosome-EF-Tu interactions, for example, the ϵ -amino group of lysine 282 in *E. coli* EF-Tu is within hydrogen-bonding distance of G382 in 16S rRNA, but not the serine at this position in *T. thermophilus* EF-Tu. Inset on left panel, overlay of the crucial β -turn^{26,74} in EF-Tu domain 2 in the free (PDB ID: 1OB2, R. C. Nielsen *et al.*, unpublished data) and ribosome-bound state from *E. coli* and *T. thermophilus*. d, Dynamics of the catalytic histidine 84 (ref. 75) of EF-Tu. A split density for the side chain of histidine 84 (data not shown) indicates the presence of two rotamers (rot1 and rot2, panel 1) in the present *E. coli* complex. In d, the *T. thermophilus* ribosome-bound EF-Tu structures^{6,26,76} (dark grey, complex as indicated) are shown with the corresponding rotamer of the present structure (red). Residues valine 20 and isoleucine 60 of the hydrophobic gate⁷⁶ are denoted; isoleucine 60 is not resolved in the kirromycin-stalled ribosome-EF-Tu complexes.



Extended Data Figure 8 | Cryo-EM densities for mobile proteins L9 and L31 and the arrangement of L9 in polysomes. Densities in **a** and **b** were obtained by semi-automatic segmentation using the 'segger' tool in UCSF CHIMERA^{41,77} and normalized and low-pass filtered according to local resolution estimates. **a**, Cryo-EM map and models of protein L9 (~ 4 Å local resolution, rendered at 1σ). **b**, Cryo-EM maps and models of protein L31 in the ground-state of the ribosome (left, ~ 4.3 Å local resolution) and in the rotated state (right, ~ 6 Å local resolution); maps were rendered at 1.5σ . **c**, Model of protein L9 in the context of polysomes. Overviews show the arrangement of neighbouring ribosomes (i-1 and i) in the major t-t form of *E. coli* polysomes as obtained by fitting the present 70S ribosome structure into the cryo-electron tomography reconstruction²⁷ in UCSF CHIMERA⁴¹. Left close-up, the conformer of L9 as seen in the present cryo-EM map (L9 cryo-EM, blue) is

located close to protein S4 of the neighbouring 30S subunit (30S i) according to the polysome model. The purple arrow indicates the rearrangement of L9 from the cryo-EM conformation to that seen in crystals. The black arrow denotes the location of the mRNA entry channel in the 30S subunit i. Right close-up, the conformer of L9 as seen in the context of ribosome crystals (L9 X-ray, pink) reaches into the ribosomal A-site of the neighbouring 30S subunit and would be compatible with the simultaneous binding of elongation factors in the polysome model. In crystals, protein L9 precludes the binding of elongation factors due to the tighter packing of ribosomes⁷⁸. The model of L9 was obtained by superposition of the *E. coli* 70S ribosome X-ray structure⁵ (PDB IDs: 4TP8 and 4TP9) onto ribosome i-1 in the polysome model using UCSF CHIMERA⁴¹.

Extended Data Table 1 | Data collection and model refinement

<i>E. coli</i> 70S ribosome-EF-Tu complex	Complete model	65% of model	43% of model	24% of model
Data collection				
Particles	417210			
Pixel size (Å)	0.75525			
Defocus range (µm)	0.7-2.5			
Electron dose (e ⁻ /Å ²)	40±5			
Reciprocal space data				
Space group	P1			
<i>a</i> , <i>b</i> , <i>c</i> (Å)*	302.1, 302.1, 302.1			
α, β, γ (°)	90.0, 90.0, 90.0			
Resolution (Å)	2.9	2.80	2.70	2.65
Wilson B (Å ²)	44.1	46.0	45.24	43.7
Refinement†				
Resolution range (Å)‡	MLHL 50.0 – 2.90 (2.95 – 2.90)	MLHL 50.0 – 2.80 (2.85 – 2.80)	MLHL 50.0 – 2.70 (2.75 – 2.70)	MLHL 50.0 – 2.65 (2.70 – 2.65)
No. Reflections	2366496 (112206)	2629133 (125775)	2932674 (139922)	3101577 (146909)
<i>R</i> _{work} §/CC _{work}	0.2411/0.922 (0.4792/0.298)	0.2217/0.940 (0.4945/0.238)	0.2328/0.937 (0.5000/0.209)	0.2318/0.939 (0.5001/0.252)
<i>F</i> _{SC} _{work} ¶	0.930 (0.541)	0.942 (0.500)	0.938 (0.529)	0.940 (0.502)
<i>ML</i> based phase error (°)	28.9	27.8	29.9	29.9
Residues with atoms out of density for main chain/side chain#	0/3	0/1	0/1	0/0
No. Atoms/RSCC★				
Protein	152719	99034	66327	36067
RNA, tRNA	49242/0.818	14939/0.824	6795/0.813	3259/0.818
Ligand, ion	103031/0.872	83922/0.873	59461/0.872	32799/0.871
B-factors (Å ²)	445	173	71	9
Protein	95.4	68.4	61.9	60.8
RNA, tRNA	110.0	74.2	66.0	69.9
Ligand, ion	88.5	67.5	61.5	59.9
R.m.s deviations	66.5	29.1	20.1	24.9
Bond lengths (Å)	0.004	0.007	0.007	0.006
Bond angles (°)	0.729	1.060	0.929	0.971
Ramachandran plot statistics				
Most favored (%)	85.59	87.4	88.56	87.53
Disallowed (%)	3.30	2.66	2.78	3.52

* For model refinement, the cryo-EM map was cropped from 420 × 420 × 420 pixels to 400 × 400 × 400 pixels.

† Refinement target: MLHL maximum likelihood with experimental phase probability distribution.

‡ Highest resolution shell is shown in parenthesis.

§ $R_{work} = \frac{\sum ||F_{EM}| - |F_{model}||}{\sum |F_{EM}|}$, where F_{EM} are structure factors calculated based on the solvent-flattened cryo-EM map and F_{model} are structure factors calculated from the refined model. The structure factors belonged to working set which was used for reciprocal space refinement.

|| CC_{work} = Pearson correlation coefficient calculated between F_{EM} and F_{model} .

¶ $F_{SC_{work}}$ is the averaged over all shells Fourier Shell Correlation ($F_{SC_{overall}}$) calculated between F_{EM} and F_{model} belonging to the working set. The value for the highest resolution shell is shown in parenthesis and was calculated using:

$$F_{SC_{work(shell)}} = \frac{\sum (F_{EM} \times F_{model} \times \cos(\Delta Phase))}{\sqrt{\sum |F_{EM}|^2} \times \sqrt{\sum |F_{model}|^2}}$$

Calculated with RESOLVE⁵⁴.

★ Residue averaged real space local correlation coefficient (RSCC) in the region of the model to the cryo-EM map calculated with RESOLVE.

Extended Data Table 2 | Comparison of densities as observed in cryo-EM and X-ray crystallography by local cross-correlation*

Method/resolution	Cryo-EM @ 2.9 Å	X-ray @ 2.95 Å	X-ray @ 2.8 Å	X-ray @ 2.8 Å
Ribosome complex	<i>E. coli</i> 70S-EF-Tu-tRNA ₃	<i>E. coli</i> 70S-EF-G	<i>E. coli</i> 70S-quinupristin	<i>T. th.</i> 70S-tRNA ₃
PDB ID		2KJ1 & 2KJ2 ⁷³	4TPA & 4TPB ⁵	2J00 & 2J01 ⁵⁰
Protein				
Map correlation in region of model	0.818	0.836	0.787	0.857
Total residues	6320	6460	5722	5909
Residues in acceptable density†	4293	5214	4019	3710
Residues with some weak density‡	2027	1246	1703	2199
Residues out of density§	3	0	0	0
Residues in very weak density	103	19	27	49
Residues in weak density¶	840	316	668	872
Main-chain out of density	0	1	0	0
Main-chain in very weak density	1	1	0	1
Main-chain in weak density	225	77	158	208
Side-chain out of density	3	3	12	2
Side-chain in very weak density	36	64	58	94
Side-chain in weak density	481	508	573	915
Avg. RSCC for Arg, His and Lys side chains	0.933	1.159	0.918	0.790
Avg. RSCC for Glu and Asp side chains	0.514	1.090	1.091	0.558
Avg. RSCC for Gln and Asn side chains	0.865	1.273	1.151	0.952
Avg. RSCC for aromatic side chains	1.320	1.551	1.260	1.324
Avg. RSCC for aliphatic side chains	0.887	0.972	0.693	0.852
RNA				
Map correlation in region of model	0.749	0.888	0.861	0.909
Total residues	4800	4505	4554	4494
Residues in acceptable density	2860	3602	3021	3573
Residues with some weak density	1940	903	1533	921
Residues out of density	2	0	0	0
Residues in very weak density	104	36	28	59
Residues in weak density	501	180	596	425
Main-chain out of density	0	0	0	0
Main-chain in very weak density	4	1	0	0
Main-chain in weak density	495	96	189	157
Side-chain out of density	0	0	0	0
Side-chain in very weak density	0	0	0	0
Side-chain in weak density	18	10	58	37

* Real space correlation coefficients (RSCCs) were calculated with RESOLVE⁵⁴ to compare the local model fit to the normalized experimental map.

† 'acceptable density': no atom lies in density <1 s.d. below 1/2 mean for that atom type and no group is <1/2 mean for that group.

‡ 'residues with some weak density': all residues which do not fulfill the requirement for acceptable density.

§ 'out of density': density level <2 standard deviations below 1/2 mean density for the particular residue.

|| 'very weak density': density level <1 s.d. below 1/2 mean density for the particular residue.

¶ 'weak density': density level <1/2 mean density for the particular residue.

Overall, the definition of protein and RNA main and side chain densities is similar between the present cryo-EM data and 70S ribosome crystal structures at similar resolutions, suggesting also a similar extent of radiation damage. The RSCC values obtained for specific amino acid side chain groups indicate different sensitivity to radiation damage for specific side chains, with negatively charged side chains being the most sensitive ones both in cryo-EM and X-ray crystallography⁶⁰⁻⁶². The elevated RSCCs calculated for the 2.95 Å *E. coli* 70S-EF-G crystal structure show the smallest fluctuations between different side chain groups and, thus, the lowest level of radiation damage, most probably owing to multi-crystal merging of 20 partial data sets. In contrast, experimental data for the 2.8 Å *E. coli* 70S-quinupristin and the 2.8 Å *T. thermophilus* 70S-tRNA crystal structures were collected from two and one crystal(s), respectively.